

Analysis of Performances for Three Massive MIMO Channel Models

Fan Lai¹, Carlos F. López², Xiqi Gao¹, Cheng-Xiang Wang^{1,2}, and Fuchun Zheng¹

¹National Mobile Communications Research Laboratory, Southeast University, Nanjing, Jiangsu 211189, China.

²Institute of Sensors, Signals and Systems, Heriot-Watt University, Edinburgh EH14 4AS, UK.

Email: lai_fan@seu.edu.cn, c.f.lopez@hw.ac.uk, {xqgao, chxwang, fzheng}@seu.edu.cn

Abstract—In this paper, we compare the performance of three different massive multiple-input-multiple-output (MIMO) channel models using key statistical properties and performance metrics such as channel correlation and capacity, respectively. The channel models studied belong to the widely-used class of geometry-based stochastic models (GBSMs). In addition, we study the influence of the elevation angles and the von Mises k-factor (angular spread) on the channel capacity predicted by two three-dimensional (3-D) GBSMs employing spherical and parabolic wavefronts, respectively. Finally, we present simulation results comparing the channel correlation of the three models and demonstrate the potential impact of the elevation angles and k-factor on the massive MIMO channel capacity.

I. INTRODUCTION

Nowadays, one of the most successful technologies is the wireless communication technology, due to the fact that wireless traffic has increased with an exponential rate over a century [1]. As an emerging technology, massive MIMO greatly scales up the magnitude of conventional MIMO compared to current state-of-art [2]. It can greatly enhance the efficiency of both the spectrum and energy versus conventional MIMO system [3].

To better analyze the performance and capability of a real massive MIMO system, accurate and efficient small-scale fading channel models are required [4]. MIMO channel models are usually sorted into two kinds: correlation-based stochastic models (CBSMs) and GBSMs [3]. Among them, conventional MIMO GBSMs include the one-ring model, double-ring model, and ellipse model [5], [6]. In the past, conventional two-dimensional (2-D) and 3-D MIMO channel models were proposed. In [7] a multiple 2-D circular-ring GBSM was employed to model cooperative MIMO systems. In [8] and [9], the cylindrical geometry was studied to model 3-D MIMO channel properties. A combined approach was used in [10] and [11] where the ellipse and two-ring models were employed to study MIMO vehicular communication systems.

In recent years, for better describing the characteristics of massive MIMO channels, such as the so-called near-field effects, a number of GBSMs were proposed. A 2-D ellipse model [4] for massive MIMO channels was proposed. In this model spherical instead of plane wavefronts were employed to capture non-stationary properties of the channel. On the other hand, a 3-D twin-cluster massive MIMO channel model [12] was proposed, which abstracted the complex scattering conditions as a virtual connection between the first and last

bounce of the propagation path. In [13], the performances of the above two models were compared. Moreover, in [14], authors proposed a new 3-D broadband parabolic wavefront model, which was able to capture near-field effects through a second-order wavefront with lower complexity as compared to that of the spherical wavefront. Other new characteristics found in recent measurements such as cluster evolution [15], [16], were considered in all these models.

Although in [4], [12], [14], the authors have already studied the statistical properties of the above-mentioned models, channel capacities predicted by these have not been investigated yet.

The reminder of this paper is organized as follows. Section II presents the 2-D ellipse model, 3-D twin-cluster model, and 3-D parabolic wavefront model for massive MIMO channels. Results and discussions are presented in Section III. Section IV concludes this paper.

II. THREE MASSIVE MIMO CHANNEL MODELS

A. 2-D Ellipse Model

In Fig. 1, the 2D broadband ellipse model is depicted including the spherical wavefront effect and the (dis)appearance of clusters over the array. A uniform linear array (ULA) with $N_T(N_R)$ equally spaced omnidirectional antenna elements at the transmitter (receiver) side is employed. The spacing between antennas is δ_T and δ_R . The receiver and transmitter antenna arrays are at a distance of $2f$ where f is the focal length of these confocal ellipses and their location are the focal points. The transmit antenna l is denoted as A_l^T and the receive antenna k is denoted as A_k^R . Cluster n exists on the ellipse n , corresponding to the major axis of length $2a_n$. The angle $\beta_T(\beta_R)$ denotes the transmit (receive) tilt angle and α_v denotes the angle between the motion direction of the receiver and the x -axis. The carrier wavelength is λ . The maximum Doppler frequency is f_{\max} .

Let $C_l^T(C_k^R)$ denote a collection of clusters which can be observed by $A_l^T(A_k^R)$. Birth-death processes are used to model the generation of C_l^T and C_k^R . In addition, let N_{total} denote the sum of the clusters which can be observed by one or more antennas at transmitter side and receiver side. Here, N_{total} is given by [12]

$$N_{\text{total}} = \text{card} \left(\bigcup_{l=1}^{N_T} \bigcup_{k=1}^{N_R} (C_l^T(t) \cap C_k^R(t)) \right) \quad (1)$$

TABLE I
MAIN PARAMETERS OF THE 2-D ELLIPSE MODEL.

Parameter	Definition
$\delta_T (\delta_R)$	transmit (receive) antenna spacing
$N_T (N_R)$	number of transmit (receive) antennas
$\beta_T (\beta_R)$	transmit (receive) tilt angles
f_{\max}	maximum Doppler frequency
λ	wavelength of the carrier
A_l^T, A_k^R	antenna l at th transmitter, antenna k at the receiver
f_{kl}^{LOS}	Doppler frequency of the LOS path from transmit antenna l to receive antenna k
$f_{n,i}$	Doppler frequency of cluster n via the path i
φ_{kl}^{LOS}	phase of the LOS path from transmit antenna l to receive antenna k
$\varphi_{kl,n,i}$	phase of cluster n between transmit antenna l and receive antenna k via the path i

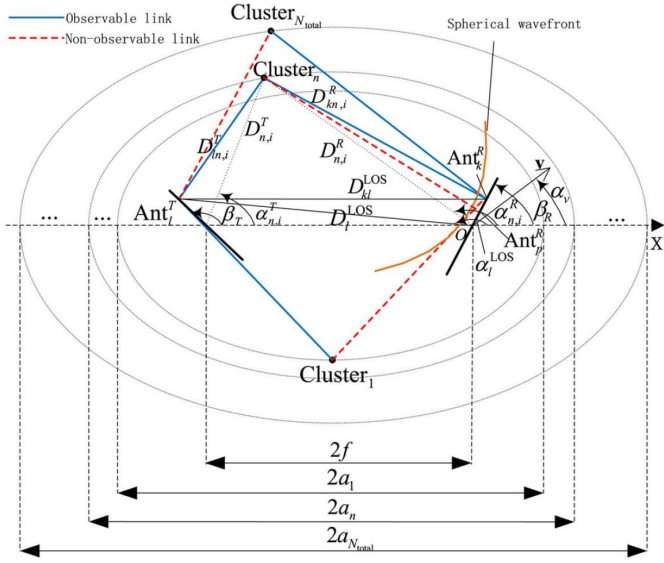


Fig. 1. 2-D ellipse model [4].

where $\text{card}(\cdot)$ represents the cardinality of a collection set. If and only if $\text{Cluster}_n \in \{C_l^T \cap C_k^R\}$, we can say cluster, $\text{Cluster}_n (n \leq N_{\text{total}})$, is observed by both A_l^T and A_k^R .

According to the analysis above mentioned and the summary of main parameters in Table I, the channel can be modeled as an $N_R \times N_T$ complex matrix $\mathbf{H}(t, \tau) = [h_{kl}(t, \tau)]_{N_R \times N_T}$, where $k = 1, 2, \dots, N_R$ and $l = 1, 2, \dots, N_T$.

The power of cluster n is denoted as P_n and one cluster counts on S subpaths or rays. The angle of arrival of the i -th path in the n -th cluster is $\alpha_{n,i}^R$ with respect to the center of the receiving array and $\alpha_{n,i}^T$ with respect to the center of the transmitting array. The parameter K denotes the Rician factor. When $S \rightarrow \infty$, the channel impulse response (CIR) of the theoretical model $h_{kl}(t, \tau)$ between A_l^T and A_k^R at delay τ can be obtained as

$$h_{kl}(t, \tau) = \sum_{n=1}^{N_{\text{total}}} h_{kl,n}(t) \delta(\tau - \tau_n) \quad (2)$$

where we model the channel gain $h_{kl,n}(t)$ of Cluster_n as

-if $\text{Cluster}_n \in \{C_l^T \cap C_k^R\}$,

$$h_{kl,n}(t) = \underbrace{\delta(n-1) \sqrt{\frac{K}{K+1}} e^{j(2\pi f_{kl}^{LOS} t + \varphi_{kl}^{LOS})}}_{\text{LOS}} + \underbrace{\sqrt{\frac{P_n}{K+1}} \lim_{S \rightarrow \infty} \frac{1}{\sqrt{S}} \sum_{i=1}^S e^{j(2\pi f_{n,i} t + \varphi_{kl,n,i})}}_{\text{NLOS}} \quad (3)$$

-if $\text{Cluster}_n \notin \{C_l^T \cap C_k^R\}$,

$$h_{kl,n}(t) = 0. \quad (4)$$

In [4], details of parameter calculations in Table I can be found.

B. 3-D Twin-Cluster Model

In the 3D twin-cluster model depicted in Fig. 2, only the first and last-bounce clusters are modeled and the propagation between them is abstracted as a virtual link. N_{total} denotes the sum of clusters in a twin-cluster channel model, and each cluster, $\text{Cluster}_n (n = 1, \dots, N_{\text{total}})$ consists of two representations, Cluster_n^T at the transmitter representing the first bounce and Cluster_n^R at the receiver side representing the last bounce. A virtual connection is modeled as the communication environment between the two delegates.

ULAs of N_T and N_R antennas are equipped at both sides. The antenna spacing is δ_T at the transmit array and δ_R at the receive array. Then, let the LOS Rician factor be K , the maximum Doppler frequency be f_{\max} , and the transmit signal starts at the phase of φ_0 . In addition, suppose that the power of cluster n is P_n and there are S_1 and S_2 paths within the representation at the transmitter and receiver. According to the analysis above and the summary of main parameters definitions in Table II, the channel matrix will be denoted as an $N_R \times N_T$ complex matrix $\mathbf{H}(t, \tau) = [h_{kl}(t, \tau)]_{N_R \times N_T}$ where $k = 1, 2, \dots, N_R$ and $l = 1, 2, \dots, N_T$. The complex CIR $h_{kl}(t, \tau)$ from transmit antenna l to receive antenna k where the time is t and delay is τ , can be calculated as

$$h_{kl}(t, \tau) = \sum_{n=1}^{N_{\text{total}}} h_{kl,n}(t) \delta(\tau - \tau_n(t)) \quad (5)$$

TABLE II
MAIN PARAMETERS OF THE 3-D TWIN-CLUSTER MODEL.

Parameter	Definition
v_E^R	receive elevation angles
v_T^R	transmit elevation angles
v_A^R	receive azimuth angles
v_A^T	transmit azimuth angles
ξ_{n,i_1}^R	receive elevation angles of the path i_1 and cluster n
θ_{n,i_1}^R	receive azimuth angles of the path i_1 and cluster n
ξ_{n,i_2}^T	transmit elevation angles of the path i_2 and cluster n
θ_{n,i_2}^T	transmit azimuth angles of the path i_2 and cluster n

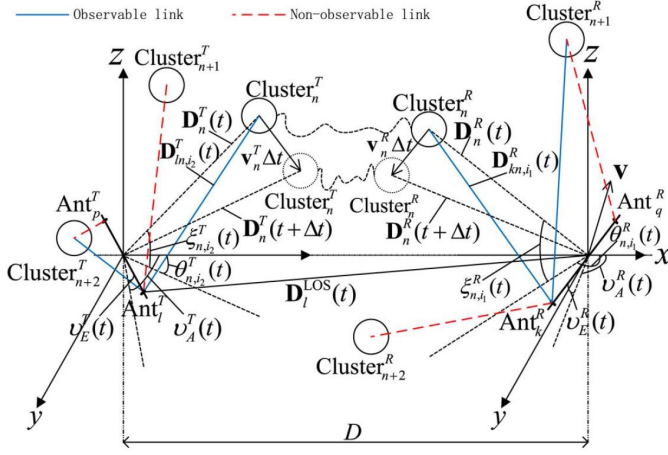


Fig. 2. 3-D twin-cluster model [12].

-if $\text{Cluster}_n \in \{C_l^T(t) \cap C_k^R(t)\}$,

$$h_{kl,n}(t) = \underbrace{\delta(n-1) \sqrt{\frac{K}{K+1}} e^{j(2\pi f_{kl}^{LOS} t + \varphi_{kl}^{LOS})}}_{LOS} + \underbrace{\sqrt{\frac{P_n}{K+1}} \lim_{S_1, S_2 \rightarrow \infty} \sum_{i_1=1}^{S_1} \sum_{i_2=1}^{S_2} \frac{e^{j(2\pi f_{kn,i} t + \varphi_{kl,n,i_1 i_2})}}{\sqrt{S_1 S_2}}}_{NLOS} \quad (6)$$

-if $\text{Cluster}_n \notin \{C_l^T(t) \cap C_k^R(t)\}$

$$h_{kl,n}(t) = 0. \quad (7)$$

In [12], details of parameter calculations in Table II can be found.

C. 3-D Parabolic Wavefront Model

Next, as depicted in Fig. 3, we consider a channel model in a 3-D space where the base station (BS) or transmitter is equipped with a ULA of N_T antennas which are equally spaced by δ_T and oriented by the elevation and azimuth angles β_T and α_T , respectively. The receiver or the mobile station (MS) is similarly equipped with N_R δ_R -spaced antennas

oriented by the elevation and azimuth angles β_R and α_R , respectively. A_p^T and A_q^R denote the transmit antenna p and the receive antenna q . Furthermore, the MS is moving at a constant speed denoted as v_R . Its moving direction is modeled by the elevation and azimuth angles ζ_R and ξ_R , respectively. The receive signal at the MS consists of the LOS components and the scattered components via C_S single-bounce clusters (SBCs) and C_M multiple-bounce clusters (MBCs).

The channel matrix is denoted as $\mathbf{H}(t, \tau) = [h_{pq}(t, \tau)]_{N_R \times N_T}$ for $p = 1, 2, \dots, N_T$ and $q = 1, 2, \dots, N_R$. The CIR $h_{qp}(t, \tau)$ consists of the LOS, SBC, and MBC elements, which can be obtained as

$$h_{qp}(t, \tau) = h_{qp}^L(t) \delta(\tau - \tau^L) + \sum_{c=1}^{C_S} h_{qp,c}^{SB}(t) \delta(\tau - \tau_c^{SB}) + \sum_{c=1}^{C_M} h_{qp,c}^{MB}(t) \delta(\tau - \tau_c^{MB}) \quad (8)$$

where LOS, SBC, and MBC components are shown in the superscripts. The propagation delays τ^L , τ_c^{SB} , and τ_c^{MB} are geometrically calculated as $\tau^L = r_L/c_0$, $\tau_c^{SB} = (r_c^{ST} + r_c^{SR})/c_0$, and $\tau_c^{MB} = (r_c^{MT} + r_c^{MR})/c_0 + \tau_{VL}$, with c_0 denoting the speed of light and τ_{VL} denoting the delay of the virtual link. The delay τ_{VL} is a random variable uniformly distributed over the interval $(\tau^L, \tau_{\max}]$, with τ_{\max} denoting the maximum delay of the virtual connection [12]

Furthermore, the LOS, SBC, and MBC elements are obtained as

$$h_{qp}^L(t) = \sqrt{P_{qp}^L(t)} e^{jk_0 D_{qp}^L(t)} \quad (9)$$

$$h_{qp,c}^{SB}(t) = \sqrt{P_{qp,c}^{SB}(t)} \lim_{I_c \rightarrow \infty} \sum_{i=1}^{I_c} a_{c,i} e^{-j(k_0 D_{qp,c,i}^{SB}(t) - \Theta_{c,i}^{SB})} \quad (10)$$

$$h_{qp,c}^{MB}(t) = \sqrt{P_{qp,c}^{MB}(t)} \times \lim_{\substack{M_c \rightarrow \infty \\ N_c \rightarrow \infty}} \sum_{\substack{m=1 \\ n=1}}^{M_c, N_c} a_{c,mn} e^{-j(k_0 D_{qp,c,mn}^{MB}(t) - \Theta_{c,mn}^{MB})} \quad (11)$$

where $k_0 = 2\pi/\lambda$, $\Theta_{c,i}^{SB}$ and $\Theta_{c,mn}^{MB}$, which are i.i.d. random variables with uniform distribution over the interval $(0, 2\pi]$,

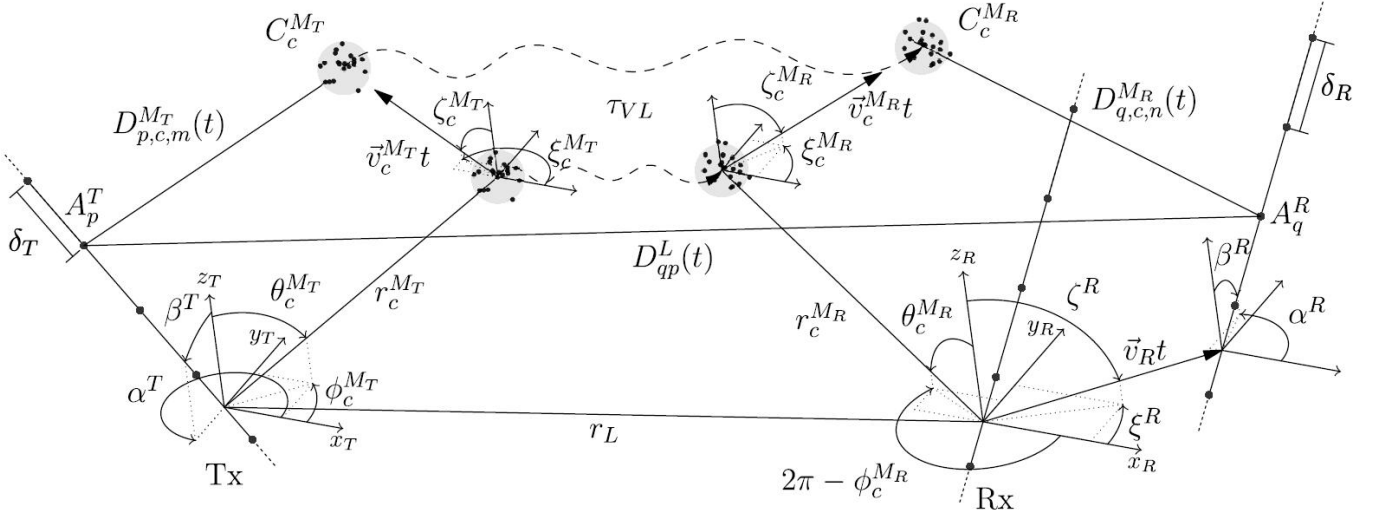


Fig. 3. 3-D parabolic wavefront model [14].

TABLE III
MAIN PARAMETERS OF THE 3-D PARABOLIC WAVEFRONT MODEL.

Parameter	Definition
δ_T, δ_R	transmit antenna spacing, receive antenna spacing
$r_c^{S_T(R)}, R_C^{M_T(R)}$	Distances from the transmitter (receiver) center to $C_c^{S_T(R)}$ and $C_c^{M_T(R)}$
$D_{p,c,i}^{S_T}, D_{q,c,i}^{S_R}$	Distances from A_p^T to $C_{c,i}^{S_T}$ and from A_q^R to $C_{c,i}^{S_R}$
$D_{p,c,m}^{M_T}, D_{q,c,n}^{M_R}$	Distances from A_p^T to $C_{c,m}^{M_T}$ and from A_q^R to $C_{c,n}^{M_R}$
r_L	Distance between the transmitter and receiver
θ_c^l, ϕ_c^l	Elevation and azimuth angles of C_c^l , where $l \in \{S_T, S_R, M_T, M_R\}$
$\theta_{c,i}^{S_T(R)}, \phi_{c,i}^{S_T(R)}$	Elevation and azimuth angles of $C_{c,i}^{S_T(R)}$
$\theta_{c,m}^{M_T(R)}, \phi_{c,m}^{M_T(R)}$	Elevation and azimuth angles of $C_{c,m}^{M_T(R)}$
θ^L, ϕ^L	Elevation and azimuth angles of the receiver versus the transmitter
ζ_c^l, ξ_c^l	Elevation and azimuth angles of the speed of C_c^l , where $l \in \{S_T, S_R, M_T, M_R\}$
ζ^R, ξ^R	Elevation and azimuth angles of the speed vector of the receiver
$\beta^{T(R)}, \alpha^{T(R)}$	Elevation and azimuth orientation angles of the transmitter (receiver)
v_c^l, v_R	Speeds of the cluster C_c^l , where $l \in \{S_T, S_R, M_T, M_R\}$ and speed of the receiver

denote the phase change caused by the scatterers. The path amplitudes $a_{c,i}$ and $a_{c,mn}$ are subject to $\mathbb{E}[a_{c,i}^2] = 1/I_c$ and $\mathbb{E}[a_{c,mn}^2] = 1/N_c M_c$, where $\mathbb{E}[\cdot]$ denotes the expectation operator. The processes $P_{qp}^L(t), P_{qp,c}^{SB}(t), P_{qp,c}^{MB}(t)$ denote the mean powers of the LOS, SBCs, and MBCs components, and they are space-time variant.

In this model, the distances between the clusters and the receiver and transmitter are approximated through a second-order Taylor polynomial that leads to the so-called parabolic wavefront of reduced complexity. Further details of this model can be found in [14].

III. RESULTS AND ANALYSIS

The normalized spatial cross correlation function(CCF) $\rho_{kl,k'l',n}(\delta_T, \delta_R, t, \Delta t)$ between the channel gains $h_{kl,n}(t)$ and $h_{k'l',n}(t)$ is defined as [12]

$$\rho_{kl,k'l',n}(\delta_T, \delta_R, t, \Delta t) = \mathbb{E} \left[\frac{h_{kl,n}^*(t) h_{k'l',n}(t + \Delta t)}{|h_{kl,n}^*(t)| |h_{k'l',n}(t + \Delta t)|} \right] \quad (12)$$

where k, l, k', l' represent the indexes of antenna elements at the transmitter and receiver. n denotes the cluster index. δ_T, δ_R represent the transmit and receive antenna spacing. t and Δt denote absolute and relative time (time difference), respectively.

Assuming the channel experiences slow fading, absolute values of cluster-level CCF of the 2-D ellipse model, 3-D twin-cluster model, and 3-D parabolic wavefront model for massive MIMO are depicted in Fig. 4. It shows that the predicted correlation function of the 3-D twin-cluster model is lower than that of the 2-D ellipse model. Furthermore, comparing with above two models, the spatial correlation of the 3-D parabolic wavefront model is the lowest. The differences between these 3-D models can be attributed to

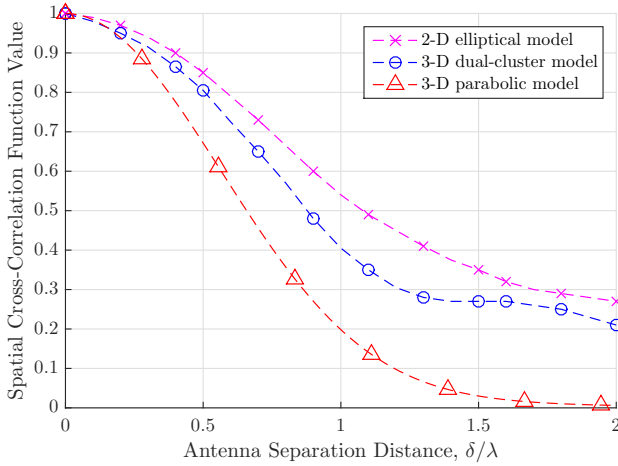


Fig. 4. Comparison of cluster-level spatial CCF of three massive MIMO channel models ($N_R = 8, N_T = 32, f_c = 2\text{GHz}, \|D\| = 100\text{m}, v_A^R = \pi/4, v_A^T = \pi/3, v_E^R = \pi/4$ (3-D models only), $v_E^T = \pi/4$ (3-D models only)).

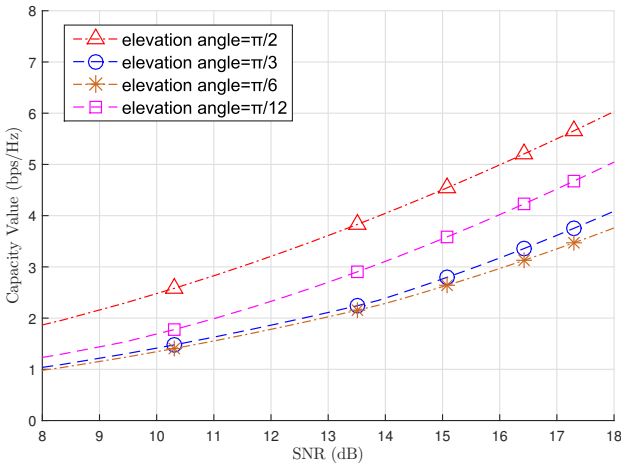


Fig. 5. Capacity comparisons for the 3-D twin-cluster model with different elevation angles of arrival (AoAs) ($N_R = 8, N_T = 32, f_c = 2\text{GHz}, \|D\| = 100\text{m}, v_A^R = \pi/4, v_A^T = \pi/3, v_E^R = \pi/4$).

both the wavefront and angular distribution of the scatterers. Whereas in [13] authors used independent elevation and azimuth von Mises distributions, authors in [14] employed a VMF distribution that jointly models elevation and azimuth angles.

Assuming slow fading, the channel may remain approximately constant long enough to allow reliable estimation of the channel state at the receiver (perfect CSIR) and timely feedback of this state information to the transmitter (perfect CSIT). The optimum input covariance matrix that maximizes ergodic capacity is the scaled identity matrix, i.e., the transmit power is divided equally among all the transmit antennas. Thus, the ergodic capacity is given by [17]

$$C = \mathbb{E}_{\mathbf{H}} \left[\log \left| \mathbf{I}_{N_R} + \frac{P}{N_T} \mathbf{H}\mathbf{H}^H \right| \right] \quad (13)$$

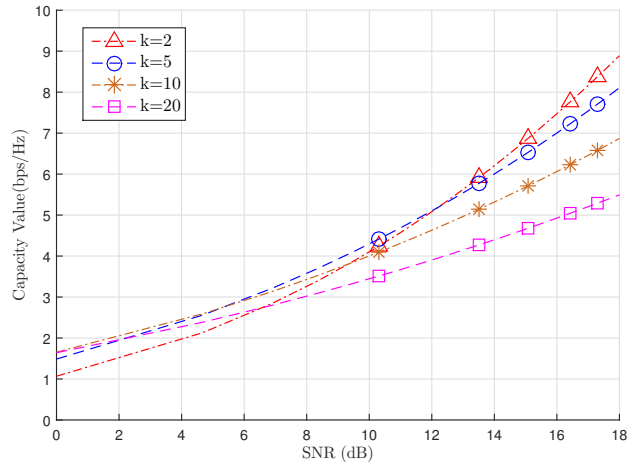


Fig. 6. Capacity comparisons for the 3-D parabolic wavefront model with different von Mises-Fisher (VMF) k -factor values ($f_c = 2\text{GHz}, N_T = 100, \delta_T = \lambda/2, \beta^T = \pi/2, \alpha^T = 0, \theta_\mu = 3\pi/4, \phi_\mu = \pi/3, \zeta_c^{MT} = \pi/6, \xi_c^{MT} = \pi/6, r_v^{MT} = 30\text{m}, v_c^{MT} = 5\text{m/s}$).

where \mathbf{H} is the channel matrix. P is the transmit power. $(^H)$ represents the conjugate transpose and $\text{Tr}(\cdot)$ represents the trace. \mathbf{I} denotes the identity matrix.

Fig. 5 compares the channel capacities for the 3-D twin-cluster model with different elevation angles of arrival. When the elevation angle equals $\pi/2$, the channel capacity is much higher than that of the rest. Furthermore, it can be observed that the capacities of all other elevation angles are very close on the low signal-to-noise ratio (SNR) regime, and the capacity reaches a minimum at the angle $\pi/6$. However, in the high SNR regime, all the capacities of different elevation angles will differ more.

The channel capacities predicted by the 3-D parabolic wavefront model with different values of VMF k -factor are depicted in Fig. 6. In the low SNR regime, the predicted channel capacity is barely affected by the angular concentration parameter as noise is the limiting factor. However, in the high SNR regime, it can be seen that larger values of the k -factor, i.e., lower angular spreads, reduce the effective channel capacity due to an increase of spatial correlation.

IV. CONCLUSIONS

In this paper, the channel capacities predicted by three massive MIMO GBMSs have been studied. An important effect on the capacities of the massive MIMO channels by the elevation angles has been demonstrated. The impact of elevation angles on the channel capacity indicates the importance of accurate 3D models. The differences in channel correlation between the 3D models studied can be attributed to both the wavefront considered and the interdependence of the elevation and azimuth angles. We have also shown that the models predict correctly the negative effect of the angular concentration parameter (inversely proportional to the angular spread) on the channel capacity.

REFERENCES

- [1] E. Björnson, E. G. Larsson, and T. L. Marzetta, “Massive MIMO: Ten Myths and One Critical Question,” *IEEE Commun. Mag.*, vol. 54, no. 2, pp. 114–123, Feb. 2016.
- [2] E. G. Larsson, F. Tufvesson, O. Edfors, and T. L. Marzetta, “Massive MIMO for next generation wireless systems,” *IEEE Commun. Mag.*, vol. 52, no. 2, pp. 186–195, Feb. 2014.
- [3] C.-X. Wang, S. B. Wu, L. Bai, X. H. You, J. Wang, and C. L. I, “Recent advances and future challenges for massive MIMO channel measurements and models,” *Sci. China Inf. Sci.*, vol. 59, no. 2, pp. 1–16, Feb. 2016.
- [4] S. Wu, C.-X. Wang, H. Haas, el-H. M. Aggoune, M. M. Alwakeel, and B. Ai, “A non-stationary wideband channel model for Massive MIMO communication systems,” *IEEE Trans. Wireless Commun.*, vol. 14, no. 3, pp. 1434–1446, Mar. 2015.
- [5] A. Ghazal, C.-X. Wang, B. Ai, D. Yuan, and H. Haas, “A non-stationary wideband MIMO channel model for high-mobility intelligent transportation systems,” *IEEE Trans. Intell. Transp. Syst.*, vol. 16, no. 2, pp. 885–897, Apr. 2015.
- [6] C.-X. Wang et al., “Cooperative MIMO channel models: A survey,” *IEEE Commun. Mag.*, vol. 48, no. 2, pp. 80–87, Feb. 2010.
- [7] X. Cheng et al., “Cooperative MIMO channel modeling and multi-link spatial correlation properties,” *IEEE J. Sel. Areas Commun.*, vol. 30, no. 2, pp. 388–396, Feb. 2012.
- [8] A. G. Zajic, G. L. Stuber, T. G. Pratt, and S. T. Nguyen, “Wideband MIMO mobile-to-mobile channels: Geometry-based statistical modeling with experimental verification,” *IEEE Trans. Veh. Technol.*, vol. 58, no. 2, pp. 517–534, Feb. 2009.
- [9] Y. Yuan, C.-X. Wang, X. Cheng, B. Ai, and D. I. Laurenson, “Novel 3D geometry-based stochastic models for non-isotropic MIMO vehicle-to-vehicle channels,” *IEEE Trans. Wireless Commun.*, vol. 13, no. 1, pp. 298–309, Jan. 2014.
- [10] X. Cheng, C.-X. Wang, B. Ai, and H. Aggoune, “Envelope level crossing rate and average fade duration of non-isotropic vehicle-to-vehicle Ricean fading channels,” *IEEE Trans. Intell. Transp. Syst.*, vol. 15, no. 1, pp. 62–72, Feb. 2014.
- [11] X. Cheng, C.-X. Wang, D. I. Laurenson, S. Salous, and A. V. Vasilakos, “An adaptive geometry-based stochastic model for non-isotropic MIMO mobile-to-mobile channels,” *IEEE Trans. Wireless Commun.*, vol. 8, no. 9, pp. 4824–4835, Sep. 2009.
- [12] S. Wu, C.-X. Wang, el-H. M. Aggoune, M. M. Alwakeel, and Y. He, “A non-stationary 3-D wideband twin-cluster model for 5G massive MIMO channels,” *IEEE J. Sel. Areas Commun.*, vol. 32, no. 6, pp. 1207–1218, June 2014.
- [13] S. Wu, C.-X. Wang, Y. Yang, W. J. Wang, and X. Q. Gao, “Performance Comparison of Massive MIMO Channel Models,” in *Proc. of ICC’16*, Chengdu, China, pp. 1–6, Jul. 2016.
- [14] C. F. Lopez and C.-X. Wang, “Novel 3D Non-Stationary Wideband Models for Massive MIMO Channels,” *IEEE Trans. Wireless Commun.*, vol. 17, no. 5, pp. 2893–2905, May 2018.
- [15] X. Gao, O. Edfors, F. Tufvesson, and E. G. Larsson, “Massive MIMO in Real Propagation Environments: Do All Antennas Contribute Equally?” *IEEE Trans. Commun.*, vol. 63, no. 11, pp. 3917–3928, Nov. 2015.
- [16] J. Hoydis, C. Hoek, T. Wild, and S. Brink, “Channel Measurements for Large Antenna Arrays,” in *Proc. of ISWCS’12*, Paris, France, Aug. 2012, pp. 811–815.
- [17] A. Goldsmith, S. A. Jafar, N. Jindal, and S. Vishwanath, “Capacity Limits of MIMO Channels,” *IEEE J. Sel. Areas Commun.*, vol. 21, no. 5, pp. 684–702, June 2003.